Mon. Not. R. Astron. Soc. **350,** 375–384 (2004) doi:10.1111/j.1365-2966.2004.07658.x

Cylindrical linear force-free magnetic fields with toroidal flux surfaces

G. J. J. Botha[1]★ and E. A. Evangelidis[2]★

[1]*Department of Applied Mathematics, University of Leeds, Leeds LS2 9JT*
[2]*Laboratory of Non-Conventional Sources of Energy, Demokritos University of Thrace, Kimeria, Xanthi, Greece*

Accepted 2004 January 21. Received 2004 January 15; in original form 2003 July 15

ABSTRACT

A linear force-free field solution is presented in cylindrical coordinates, formulated in terms of trigonometric and Bessel functions. A numerical exploration has revealed that this solution describes magnetic field lines that meander in Cartesian space, as well as field lines that lie on toroidal flux surfaces. These tori are in (or close to) the plane perpendicular to the cylindrical axis. Nested tori, as well as tori with shells that have finite thickness, were found. The parameter space of the solution shows that the tori exist within a bounded range of values.

Key words: magnetic fields – MHD – Sun: corona – solar wind.

1 INTRODUCTION

Magnetic fields and plasmas play a dominant role in the solar environment and interplanetary space (Phillips 1992; Aschwanden, Poland & Rabin 2001). The plasma β, which is the ratio of the gas over magnetic pressure, characterizes the physics that describes the behaviour of the plasma. For low β plasmas, such as in the corona (Golub & Pasachoff 1997) and parts of the solar wind (Osherovich, Farrugia & Burlaga 1993; Hundhausen 1995), magnetic field effects dominate. It is known that a plasma in a closed volume with perfectly conducting boundaries will relax to its minimum energy in the presence of a small amount of diffusivity, under the constraint that global helicity is conserved. This minimum state is given by linear force-free fields (Woltjer 1958; Chandrasekhar & Woltjer 1958; Taylor 1974). This property of linear force-free fields ensures their appeal when describing plasmas with low β values in a diverse range of studies in solar physics, astrophysics, as well as laboratory (fusion) plasmas (see Clegg et al. 2000a,b, and references therein). It is difficult to find bounded solutions in R^3 for linear force-free magnetic fields, described by the equation

$$\nabla \times \boldsymbol{B} = k\boldsymbol{B}, \tag{1}$$

where $\boldsymbol{B}$ is the magnetic field and k is a constant. Only two solutions have been identified in three-dimensional (3D) Cartesian space, both of which are periodic in all three directions. The first was discovered by Arnold (1965) and it is only recently that the integral of energy for this solution was found (Evangelidis, Vaughan & Botha 2000). A second solution was discovered by the present authors (Evangelidis & Botha 2003), with its own integral of energy. So far, no other bounded solutions are known in 3D Cartesian space which are not trivially reduced to Arnold's solution.

To find analytical solutions in more complicated geometries, it is usual to impose some symmetry on the problem (Marsh 1996). In the case of cylindrical coordinates, the 2π periodicity of the poloidal angle θ around the z-axis helps to simplify the mathematical expressions. Cylindrical coordinates are a natural system to use as a first approximation of coronal loops. Observations have shown that these loops have axially uniform cross-sections (Bellan 2003). Their very small inverse aspect ratios are often used to justify the neglect of curvature and to model them as straight cylinders, which is known as the thin flux tube approximation (see Zhugzhda 1996; Van der Linden & Hood 1999; Lothian & Browning 2000, and references therein). Coronal loops are line-tied to the photosphere (Berger 1991). As such, boundary conditions at the ends of the cylindrical axis are important, as the coronal physics are influenced by conditions at the photosphere and chromosphere (Aschwanden, Nightingale & Alexander 2000). As the solar wind moves away from the Sun, it carries the coronal flux tubes along with it. More specifically, coronal mass ejections (Low 2001) form solar flux ropes (also known as interplanetary magnetic clouds) as they move in the solar wind away from the Sun. Usually the plasma $\beta \ll 1$ for these flux ropes (Burlaga 1988), and Shimazu & Vandas (2002) have shown that as the flux ropes expand due to the ambient pressure decrease with distance from the Sun, they maintain a force-free state. As such, the flux ropes are modelled locally as infinitely long cylinders described by linear force-free magnetic fields (Burlaga 1988; Lepping et al. 2001; Berdichevsky, Lepping & Farrugia 2003). Cylinders have also been used to describe linear force-free magnetohydrostatic equilibria in the small inverse aspect ratio limit of tokamak plasmas (Lortz & Spies 1994). In this case, the imposed boundary condition is periodicity along the z-axis.

Lundquist (1950) was first to write a linear force-free solution in cylindrical coordinates. His solution is given by

$$B_r = 0, \qquad B_\theta = AJ_1(kr), \qquad B_z = AJ_0(kr), \tag{2}$$

where A is a constant and the k in the Bessel function arguments is from equation (1). This solution describes a helical field, where the field line pitch changes with radius r. It has been used extensively in the literature (Farrugia, Osherovich & Burlaga 1995). Vandas &

★E-mail: gert@maths.leeds.ac.uk (GJJB); eevangel@env.duth.gr (EAE)

Romashets (2003) generalized the Lundquist solution for the case of an oblate cylinder, writing the answer in terms of the even and the modified even Mathieu function of order zero.

The non-linear, i.e. $k = k(r)$ in equation (1), force-free field of Gold & Hoyle (1960) is the only non-linear solution we specifically mention in this short overview of cylindrical solutions to equation (1). The reason for this is the similarities it has with the Lundquist solution. It is given by

$$B_r = 0, \qquad B_\theta = \frac{B_0 \mu r}{1 + (\mu r)^2}, \qquad B_z = \frac{B_0}{1 + (\mu r)^2}, \tag{3}$$

which satisfy equation (1) when $k = 2\mu/[1 + (\mu r)^2]$. This solution is uniform in θ and z, and a field line remains at the same radial distance r as in the Lundquist solution. However, in this case all the field lines have uniform twist, in that each field line rotates through the same angle θ per unit length along the axis. In the formulation used here, the length along the z-axis for one rotation is $2\pi/\mu$, where μ is a number. This field has been used and generalized subsequently by Low (1977) and Low & Berger (2003).

The momentum equation of ideal magnetohydrodynamics (MHD) can be written as

$$(\nabla \times \boldsymbol{B}) \times \boldsymbol{B} = \mu_0 \nabla p \tag{4}$$

under static equilibrium conditions, where p is the gas pressure and μ_0 is the vacuum permittivity. In cylindrical coordinates and assuming axisymmetry ($\partial/\partial\theta = 0$), the magnetic field can be written as $rB_r = -\partial\psi/\partial z$ and $rB_z = \partial\psi/\partial r$, where the flux function $\psi = rA$, with A the θ component of the vector potential. Using this magnetic field, equation (4) becomes (Nishikawa & Wakatani 1994)

$$\triangle^* \psi + f \frac{\partial f}{\partial \psi} + r^2 \frac{\partial g}{\partial \psi} = 0, \tag{5}$$

with

$$\triangle^* \psi = \frac{\partial^2 \psi}{\partial z^2} + \frac{\partial^2 \psi}{\partial r^2} - \frac{1}{r}\frac{\partial \psi}{\partial r} \tag{6}$$

and where both $f = f(\psi)$ and $g = g(\psi)$ – the current and pressure terms – are arbitrary functions of the flux function $\psi = \psi(r, z)$. Equation (5) is known as the Grad–Shafranov equation, with the first two terms originating from the left-hand side of equation (4) and the third term from the right-hand side of equation (4). The Grad–Shafranov equation is a member of the family of Gegenbauer equations (Evangelidis 1982). To solve it (usually numerically), we have to define $f(\psi)$ and $g(\psi)$ and then solve $\psi(r, z)$ as a boundary value problem. Solutions of this equation show nested flux surfaces that correspond to MHD equilibria, and it is used in the control of plasma discharges in tokamaks during experiments (Ferron et al. 1998). By choosing $g(\psi) = 0$, i.e. $\nabla p = 0$ in equation (4), the magnetic field becomes force free. Solving for different functional forms of $f(\psi)$ leads to different classes of linear and non-linear force-free magnetic fields (Priest 1982; Martynov & Medvedev 2002).

The rotation of equation (1) leads to the vectorial Helmholtz equation. Hansen (1935) gave its solution in terms of three linear independent vectors, and Chandrasekhar (1956) and Chandrasekhar & Kendall (1957) used these expressions to write a solution for equation (1) in spherical coordinates. In cylindrical coordinates the solution takes the form

$$\boldsymbol{B} = k^{-1} \nabla \times \boldsymbol{M} + \boldsymbol{M}, \qquad \text{with} \quad \boldsymbol{M} = \nabla \times (f\hat{\boldsymbol{z}}), \tag{7}$$

where f satisfies the scalar Helmholtz equation. Choosing a $\cos(n\theta \pm k_0 z)$ dependence for f, the radial dependence of f is written in terms of Bessel functions (Evangelidis & Botha 2001). A $\cos[n(\theta - k_0 z)]$ dependence for f gives a radial dependence in terms of modified Bessel functions (Barberio-Corsetti 1973).

We move away from cylindrical coordinates in order to mention three important methods closely related to the above, which are used in calculating linear force-free fields in the solar corona. The photosphere is considered to be an infinite plane, and equation (7) is written in Cartesian coordinates with the z-axis perpendicular to the photosphere. Magnetograms of the photospheric magnetic field are the boundary conditions for these calculations. Chiu & Hilton (1977) derived the Green function for linear force-free fields by writing the function f in equation (7) as an integral over the infinite photospheric plane, containing the normal magnetic field and the Green function. Today, the Green function methods are important in modelling coronal field structures (Wang, Yan & Sakurai 2001; Petrie & Lothian 2003). Fourier methods provide another class of coronal magnetic field solutions. In this case f in equation (7) is written as a Fourier expansion with an $\exp[\mathrm{i}\boldsymbol{k}_\perp \cdot \boldsymbol{r}_\perp - z\sqrt{k_\perp^2 - k^2}]$ dependence, where $\boldsymbol{k}_\perp$ and $\boldsymbol{r}_\perp$ are the wave and position vectors on the photosphere and k is the parameter in equation (1) (Nagakawa & Raadu 1972). A third class of methods involve writing equation (1) in terms of Fourier transforms (Alissandrakis 1981). An overview of these methods is provided by Sakurai (1989) and they are compared and discussed by Gary (1989) and Aly (1992).

The Fourier method lends itself to solutions of equation (1) in cylindrical coordinates, where the periodicity in θ leads to the natural choice of an $\exp(\mathrm{i}\theta)$ dependence. Manheimer & Lashmore-Davies (1989) assumed periodicity in the z-direction as well, and showed that equation (1) gives the solution we use in this paper, under the constraint of a divergence-free magnetic field. In the next section, we present a short alternative derivation of that solution, and discuss some of its properties. The paper continues with a numerical investigation of the magnetic field lines and flux surfaces generated by the solution. The field lines were traced using a standard Runge–Kutta integration routine. We found field lines that are open as well as field lines lying on toroidal flux surfaces, as shown in Section 3. In Section 4 we investigate these flux surfaces, before concluding the paper with a short summary.

2 CYLINDRICAL SOLUTION

The force-free magnetic field equation (1) is written in cylindrical coordinates in the form

$$\frac{1}{r}\frac{\partial B_z}{\partial \theta} - \frac{\partial B_\theta}{\partial z} - kB_r = 0, \tag{8}$$

$$\frac{\partial B_r}{\partial z} - \frac{\partial B_z}{\partial r} - kB_\theta = 0, \tag{9}$$

$$\frac{1}{r}\frac{\partial}{\partial r}(rB_\theta) - \frac{1}{r}\frac{\partial B_r}{\partial \theta} - kB_z = 0, \tag{10}$$

with the magnetic field vector defined as $\boldsymbol{B} = (B_r, B_\theta, B_z)$. We then cross-differentiate the θ and z components of equations (9) and (10) in order to eliminate B_r, and obtain

$$\frac{\partial}{\partial z}\frac{1}{r}\frac{\partial}{\partial r}(rB_\theta) - \frac{1}{r}\frac{\partial}{\partial \theta}\frac{\partial B_z}{\partial r} - \frac{k}{r}\frac{\partial B_\theta}{\partial \theta} - k\frac{\partial B_z}{\partial z} = 0. \tag{11}$$

Differentiating equation (8) with respect to z and multiplying equation (9) by k allows us to eliminate B_r between them. This procedure gives

$$\frac{\partial}{\partial z}\frac{1}{r}\frac{\partial B_z}{\partial \theta} - \frac{\partial^2 B_\theta}{\partial z^2} - k\frac{\partial B_z}{\partial r} - k^2 B_\theta = 0. \tag{12}$$

In order to solve the system of equations (11) and (12), we assume that B_θ and B_z can be separated into a radial part and a second function of (θ, z) only. The form of this function will be determined by the physics of the problem to be modelled, as well as the desired mathematical properties of the solution. In the rest of this paper, we employ a trigonometric dependence on θ and z. With the assumptions

$$B_\theta = f(r)\cos(k_0 z - m\theta), \tag{13}$$

$$B_z = g(r)\cos(k_0 z - m\theta), \tag{14}$$

equation (12) leads to the result

$$f = \frac{k}{k_0^2 - k^2}\left(\frac{\partial g}{\partial r} - \frac{mk_0}{kr}g\right). \tag{15}$$

By substituting this, together with assumptions (13) and (14) into equation (11), the Bessel equation is obtained for the radial dependence of the function g, namely

$$\frac{\partial^2 g}{\partial r^2} + \frac{1}{r}\frac{\partial g}{\partial r} + \left(\kappa^2 - \frac{m^2}{r^2}\right)g = 0, \tag{16}$$

the solution of which is written in terms of Bessel functions, $g = \sum_{m=0}^{\infty} C_m J_m(\kappa r)$, with $\kappa^2 = k^2 - k_0^2$, and where C_m is the constant of integration to be determined by the boundary values of the problem. Substituting assumptions (13) and (14) into equation (8), and using result (15), we obtain an expression for B_r. Thus, the final expression for the magnetic field components can be written as

$$B_r = -\frac{k_0}{\kappa^2}\left(\frac{\partial g}{\partial r} - \frac{mk}{rk_0}g\right)\sin(k_0 z - m\theta), \tag{17}$$

$$B_\theta = -\frac{k}{\kappa^2}\left(\frac{\partial g}{\partial r} - \frac{mk_0}{rk}g\right)\cos(k_0 z - m\theta), \tag{18}$$

$$B_z = g\cos(k_0 z - m\theta), \tag{19}$$

or in terms of Bessel functions

$$B_r = -\frac{k_0}{\kappa}\sum_{m=0}^{\infty} C_m\left[\frac{m}{\kappa r}\left(1 - \frac{k}{k_0}\right)J_m - J_{m+1}\right]\sin(k_0 z - m\theta), \tag{20}$$

$$B_\theta = -\frac{k}{\kappa}\sum_{m=0}^{\infty} C_m\left[\frac{m}{\kappa r}\left(1 - \frac{k_0}{k}\right)J_m - J_{m+1}\right]\cos(k_0 z - m\theta), \tag{21}$$

$$B_z = \sum_{m=0}^{\infty} C_m J_m \cos(k_0 z - m\theta), \tag{22}$$

where $J_m = J_m(\kappa r)$. Any combination of terms in this series solution is a solution to the linear equation (1).

This model does not describe a finite flux tube: it has no outer radial boundary. Even though this solution is well behaved when $r \to \infty$, it may be convenient to impose a radial boundary at a finite distance a_r. In this case we have to take extra precautions to satisfy the physics (Salingaros 1990). In a laboratory plasma, it is necessary to take into account the confining magnetic field, as well as the physics at the scrape-off layer of the confinement device (Stangeby 2000). For space plasmas the magnetic flux tube is embedded in the surrounding plasma (Zhugzhda 1996). The usual physical constraints are conservation of magnetic flux and pressure balance across the radial boundary. Vandas, Romashets & Watari (2003) balance the outside gas pressure with the total pressure inside the tube, while Low & Berger (2003) embed a rope of helically symmetric force-free magnetic fields in an external field such that force balance is assured. Schönfelder & Hood (1995) placed a finite flux tube in a potential field that is well behaved at infinity. As these examples show, the matching at the free radial boundary of the linear force-free field inside the cylinder with an equal field on the outside is not a trivial problem (Low 1996), and we will not treat it here.

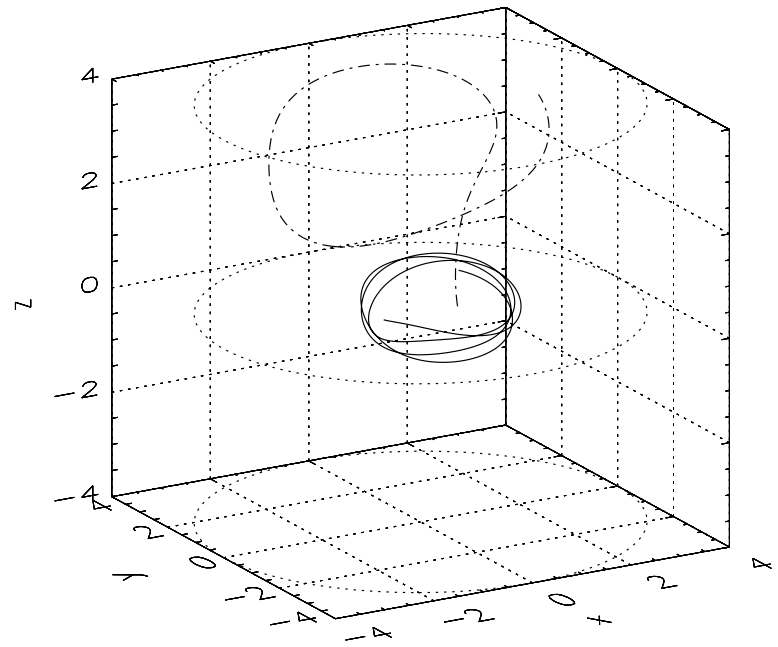

Figure 1. Two field lines showing two types of behaviour. The field line initialized at $(r, \theta, z) = (0.75, \pi, 0)$ remains on the surface of a torus. This field line is drawn as a solid line, and it is followed for 3.5 revolutions in an anticlockwise direction around the z-axis. The second field line (dot-dashed line) is initialized at coordinates (0.75, 0, 0) and is an open field line. It is drawn until it passes a_z in the z-direction.

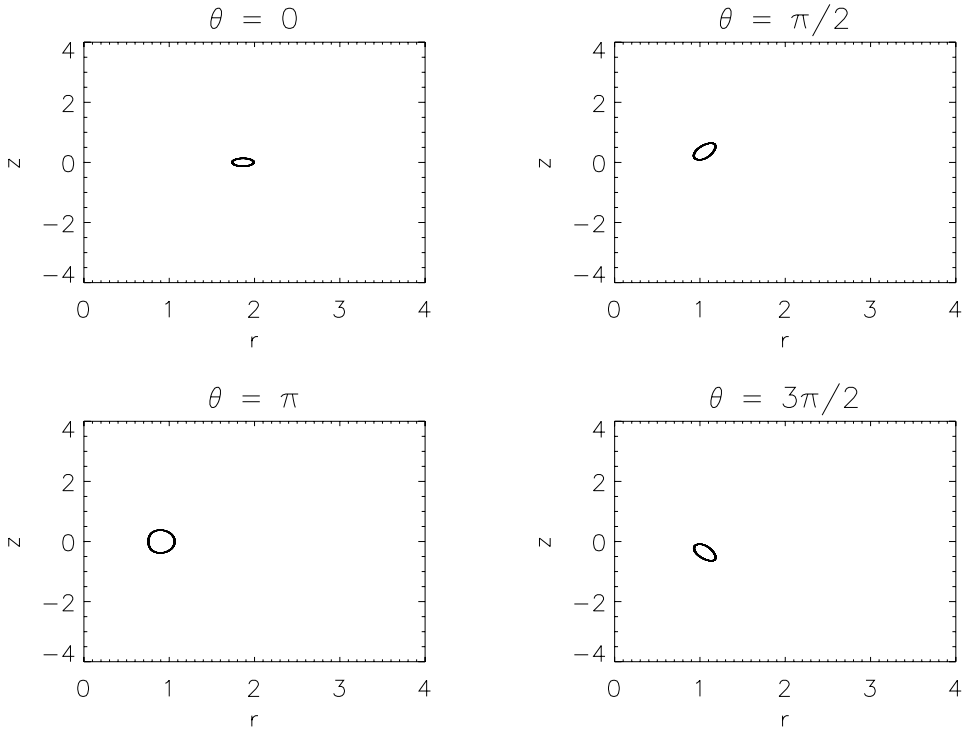

Figure 2. The field line on the toroidal surface in Fig. 1 revolves in an anticlockwise direction around the z-axis. Here it is followed for 10^3 revolutions, with the (r, z) planes drawn at four different values of the angle θ.

3 FIELD LINE TRACING

We define a cylinder, and then follow different field lines inside it. For numerical purposes the radius of the cylinder is chosen as $a_r = 4$, and the length is considered from $-a_z$ to a_z, where $a_z = 4$. We are using dimensionless quantities throughout this numerical analysis. Using the solution (20)–(22) with a fourth-order Runge–Kutta integration routine, we are able to trace different magnetic field lines inside this cylinder. The cylinder can be made periodic along the z-axis by choosing appropriate values of k_0. In this study periodicity was not imposed, so that we have an infinite cylinder.

Fig. 1 shows two field lines, traced from $\theta = \pi$ and 2π on the $z = 0$ plane at radius $r = 0.75$. They were obtained with $k_0 = 3\pi/2a_z$, $k = 2.5$, and $C_m = 1$ with $m = 0, 1, 2, \ldots, m_{\rm top}$. For $m_{\rm top} = 7$ the solution changes less than one unit of the fourth decimal place, and for $m_{\rm top} = 10$ it changes less than one unit of the sixth decimal place. All the numerical results of this paper were produced with $m_{\rm top} = 10$. The two field lines in Fig. 1 show different field topologies in the cylinder. One field line lies on the surface of a torus that has its major axis in the direction of the z-axis. The field line covers the whole of the toroidal surface as it revolves around the z-axis. This is illustrated in Fig. 2 where four (r, z) planes are drawn at angles $\theta = 0, \pi/2, \pi, 3\pi/2$. It shows that the shape of the minor cross-section of the torus is a function of the angle θ. This is especially clear when comparing the shape at $\theta = 0$ with that at $\theta = \pi$. There is also a suggestion that the shape of the minor cross-section precesses as the field line moves around the z-axis, as can be seen by comparing angles $\theta = 0$, $\theta = \pi/2$ and $\theta = 3\pi/2$. The second field line in Fig. 1 meanders around inside the cylinder and eventually leaves this section of cylinder at $z = a_z$. All the field lines of solution (20)–(22) can be classified as either lying on a toroidal surface or as open. The term open is used advisedly; field lines will eventually close on themselves in a periodic cylinder. In the remainder of this paper we will concern ourselves with the field lines lying on a toroidal surface.

4 FIELD LINES ON CLOSED TOROIDAL SURFACES

Next we investigate the dependence of the toroidal surfaces on the integration coefficients C_m in solution (20)–(22). The C_m were chosen to be equal to produce Fig. 1. As m increases, the amplitude of the Bessel functions becomes smaller, so that the values of C_m are of less importance for high values of m. By doubling the value of one coefficient at a time, we were able to trace the influence of each term on the solution. For $m \geqslant 5$ the tori survive, but their size and shape changes. The changes are more radical for lower m values. For $m \leqslant 4$ the tori are destroyed and we only found open field lines. When all the integration coefficients have different values, the tori exist provided that the C_m values do not vary more than $C_k \pm 0.5$ for the lower values of m, where C_k is the mean value of the coefficients.

By changing the value of k_0, we change the number of wavelengths fitted into the length a_z. Thus, we do not change the nature of the solution – only its scale. Finn, Guzdar & Usikov (1994) have shown that the solution of equation (1) in Cartesian coordinates, with boundary conditions corresponding to the solar photosphere, depends on the value of k; the kinking and knotting of the field lines increase as k increases. It comes as no surprise that the existence of the tori depends on the value of k. By integrating equation (1) over a surface, it is easy to show that k is the ratio of the amount of magnetic field along a closed curve C, over the amount of field passing through the surface bounded by C (Golub & Pasachoff 1997). Thus, in a sense the constant k is an indicator of the twist in the field. The k in our solution is linked to the value of k_0 through the relation

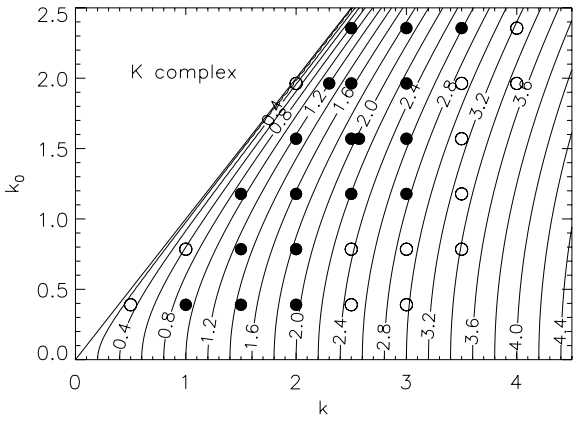

Figure 3. The parameter space of κ. The values of k and k_0 (which define κ) are plotted on the two axes, and the values of κ are represented by the contour lines. For $k < k_0$ the value of κ is complex, which we have ignored in this study. For real values of κ, the numerical runs where toroidal surfaces were found are marked with black circles, and runs where no tori were found are marked with open circles.

$\kappa^2 = k^2 - k^2{}_0$. We found it more appropriate to consider the parameter space of κ in order to investigate the existence of tori. Fig. 3 shows the parameter space of κ. For low values of k, we did not find any field lines lying on toroidal surfaces. The field line structures closest to those lying on toroidal surfaces were lines that spiral around the z-axis with varying radius r. The values of k_0 and k for which we searched are indicated in Fig. 3 by the open circles for $\kappa \leqslant 0.619$. The numerical search at these κ values was problematic, because we were forced to use a very small integration step. It is possible that we did not follow some of the field lines far enough to be absolutely sure that they do not lie on toroidal surfaces. We did find that the field lines are less kinked than for the high values of κ (or equivalently k). For $\kappa \to 0$ the solution (20)–(22) is dominated by the r and θ components, each of which is dominated by the terms

$$B_r \approx -\frac{k_0}{\kappa^2 r} \sum_{m=0}^{m_{\rm top}} C_m m \left(1 - \frac{k}{k_0}\right) J_m \sin(k_0 z - m\theta), \tag{23}$$

$$B_\theta \approx -\frac{k}{\kappa^2 r} \sum_{m=0}^{m_{\rm top}} C_m m \left(1 - \frac{k_0}{k}\right) J_m \cos(k_0 z - m\theta), \tag{24}$$

respectively. Thus, the field lines tend to move close to the (r, θ) plane, apart from the few values of θ when B_r vanishes. Then the z component (22) has a small contribution. In contrast, when κ is very large, the z component (22) dominates the solution. The field lines then tend to move mainly in the z-direction, with small contributions from the r and θ components. To obtain field lines that lie on toroidal surfaces, the three components (20)–(22) have to be of the same order, which would explain the range of κ values in Fig. 3 where these toroidal surfaces occur. The topology of the field lines changes as the value of κ changes. For a fixed value of k_0, the number of tori found decreased with an increase in the value of κ, until κ becomes so large that no tori exist. In order to show these changes more explicitly, four magnetic field lines are traced, starting on the plane $z = 0$ as shown in Fig. 4. This particular (r, θ) plane was chosen to place the starting points of the field lines in the following figures at the centre of the cylindrical section under consideration. Other values of z give similar results. Figs 5–11 show the four field lines for different values of k (and hence κ).

Fig. 5 shows the field lines for a value of $k = 2.3$ or $\kappa = 1.198$. The field line started at $\theta_0 = 0$ leaves this section of the cylinder at

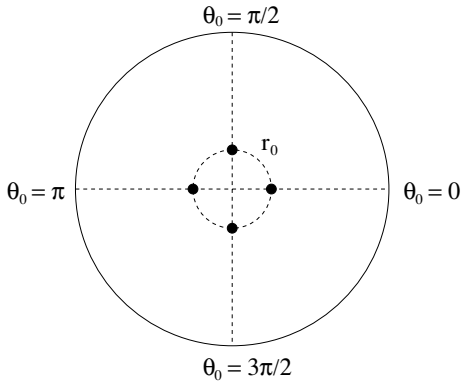

Figure 4. The initialization template on the plane perpendicular to the z-axis, at $z_0 = 0$. Field lines are traced starting at each of the black dots at radius $r_0 = a_r/4$, with $k_0 = 5\pi/2a_z$.

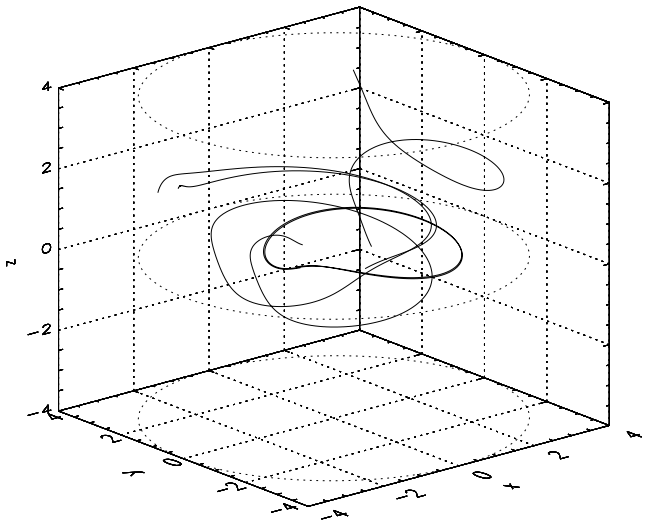

Figure 5. Initialization of Fig. 4 with $k = 2.3$, i.e. $\kappa = 1.198$.

$z = a_z$. The field line initialized at $\theta_0 = \pi/2$ rotates twice around the z-axis before it veers off. The field line at $\theta_0 = \pi$ lies on the surface of a torus that has a minor radius of approximately 0.04 length units. The field line initialized at $\theta_0 = 3\pi/2$ does not rotate around the z-axis, but follows the field line started at $\theta_0 = \pi/2$ closely. By increasing the value of κ, the shape of the four magnetic field lines change as well. Fig. 6 shows the field lines for $k = 2.5$ and $\kappa = 1.547$. The field line initialized at $\theta_0 = 0$ still leaves the cylindrical section at $z = a_z$, and the line initialized at $\theta_0 = \pi$ lies on the surface of a torus, which this time has a minor radius of approximately 0.1 length units. The field line initialized at $\theta_0 = \pi/2$ rotates twice around the z-axis before it veers off (as in Fig. 5), but the field line initialized at $\theta_0 = 3\pi/2$ now rotates 8.5 times around the z-axis before it veers off in the same direction as the line initialized at $\theta = \pi/2$.

Fig. 7 shows the field lines for $k = 3$ and $\kappa = 2.269$. The field line initialized at $\theta_0 = 0$ still leaves the cylindrical section at $z = a_z$, but the other three field lines change their behaviour dramatically. In contrast to the previous figures, the field line initialized at $\theta_0 = \pi$ now rotates only six times around the z-axis before veering off and leaving the cylindrical section at $z = a_z$. The field lines initialized

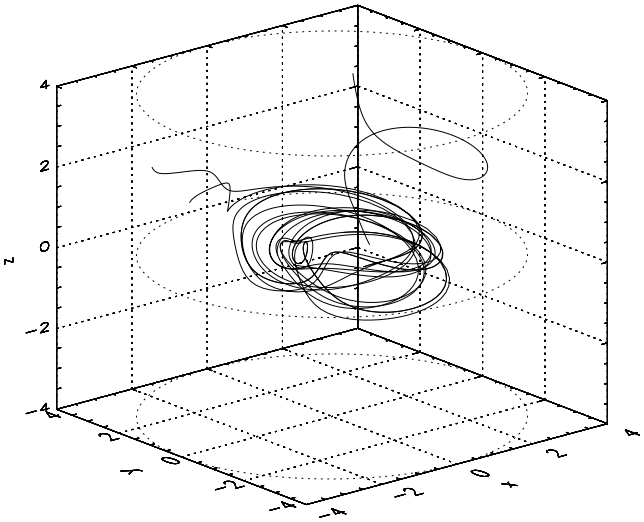

Figure 6. Initialization of Fig. 4 with $k = 2.5$, i.e. $\kappa = 1.547$.

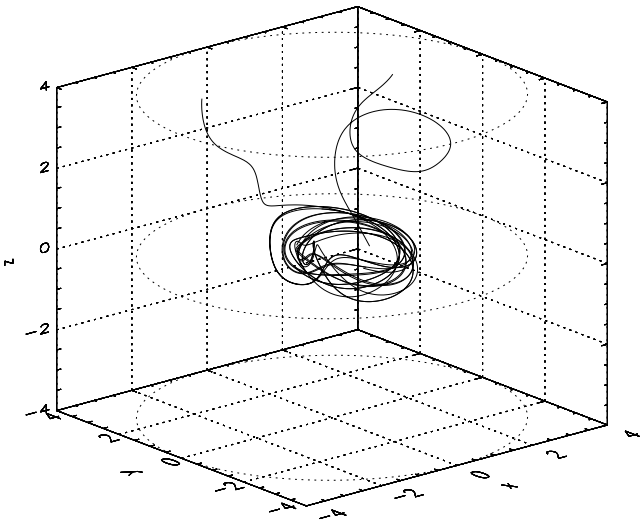

Figure 7. Initialization of Fig. 4 with $k = 3.0$, i.e. $\kappa = 2.269$.

at $\theta_0 = \pi/2$ and $\theta_0 = 3\pi/2$ both lie on the surface of tori, each with a minor radius of approximately 0.25 length units.

By increasing the value of k further to 3.25 (Fig. 8), all the tori formed by the field lines considered in the previous figures are destroyed. The field lines initialized at $\theta_0 = \pi/2$, $\theta_0 = \pi$ and $\theta_0 = 3\pi/2$ all meander around in the section of the cylinder we are considering, following one another in close proximity. The field line initialized at $\theta_0 = 0$ leaves the cylindrical section at $z = a_z$. For larger values of k we did not find any tori in the cylinder. Figs 9–11 show the paths of the field lines for $k = 3.5$, 3.75 and 4, respectively. The different values of k lead to different paths for the four field lines initialized as in Fig. 4. In Fig. 9 the field lines initialized at $\theta_0 = \pi/2$, $3\pi/2$ and 0 all leave the cylindrical section at $z = -a_z$, with lines $\theta_0 = \pi$ and $\theta_0 = 3\pi/2$ so close together at $z = -a_z$ that they are indistinguishable on our plot. In Fig. 10 all four field lines leave the cylindrical section at $z = -a_z$, and in Fig. 11 field lines $\theta_0 = 0$ and $\theta_0 = \pi/2$ leave the cylindrical section at $z = a_z$, while field lines $\theta_0 = \pi$ and $\theta_0 = 3\pi/2$ leave the section of cylinder at $z = -a_z$. The difference in the κ value used in Figs 8–11 is not large

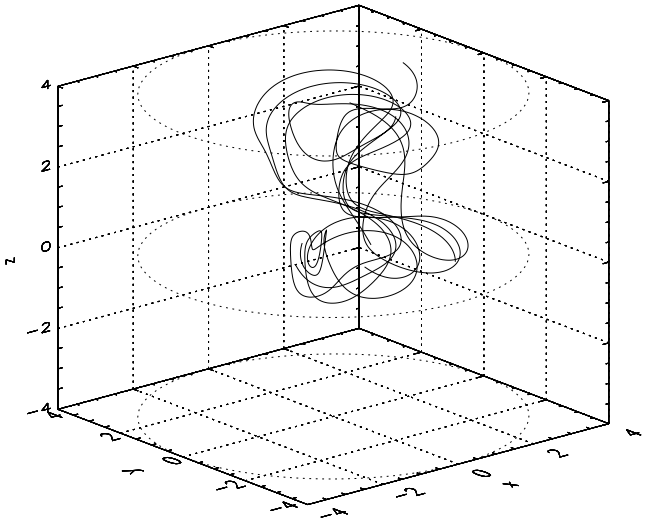

Figure 8. Initialization of Fig. 4 with $k = 3.25$, i.e. $\kappa = 2.59$.

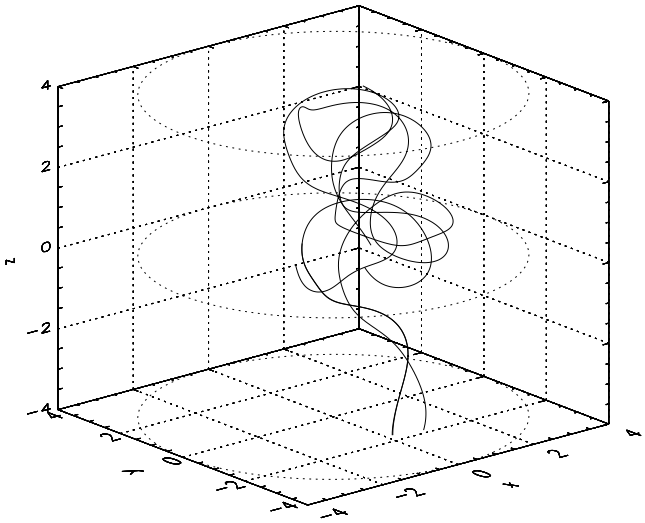

Figure 9. Initialization of Fig. 4 with $k = 3.5$, i.e. $\kappa = 2.897$.

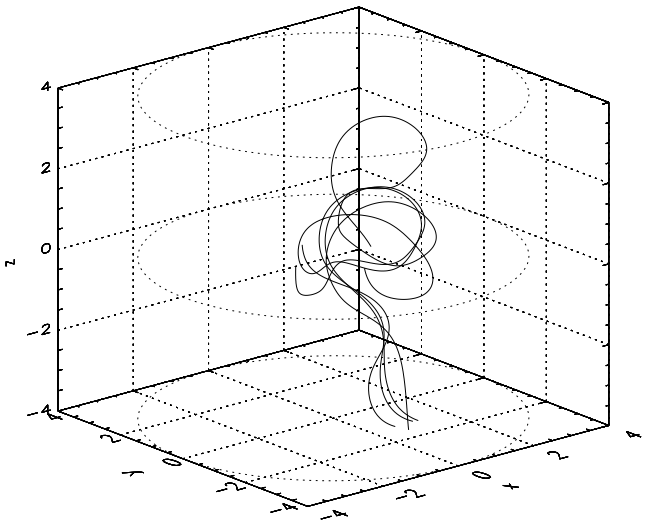

Figure 10. Initialization of Fig. 4 with $k = 3.75$, i.e. $\kappa = 3.195$.

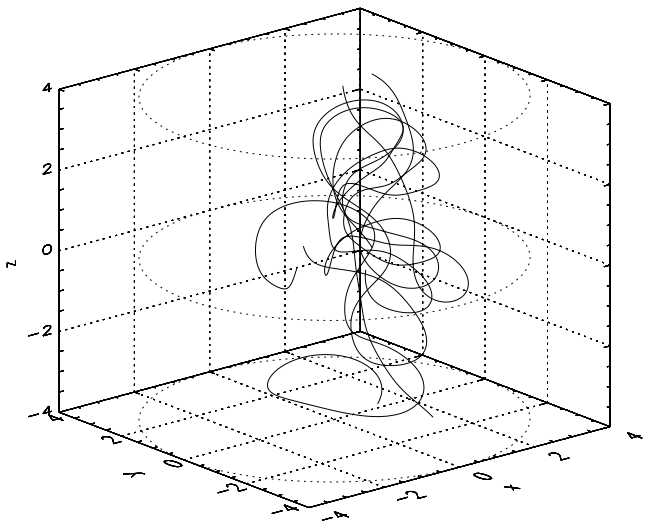

Figure 11. Initialization of Fig. 4 with $k = 4.0$, i.e. $\kappa = 3.485$.

enough to show that the field lines become more kinked and knotted as k increases. All we can say is that the toroidal surfaces, on which some field lines lie for lower values of k, seem to disappear for these higher values of k. The κ values of Figs 5 and 11 differ enough to show the effect of the size of κ on the kinkedness and knottedness of the field lines.

The magnetic field lines do not reconnect, which means that when a field line lies on a toroidal surface, it effectively divides the coordinate space into two parts. All the field lines inside the toroidal volume remain there, while everything outside remains outside. This leads to the phenomenon of nested tori. We have found several examples of nested toroidal surfaces in our numerical scan of the cylindrical section, one of which is presented in Fig. 12. It was obtained with values $k_0 = \pi/2a_z$, $k = 1$, $\kappa = 0.92$ and $C_m = 1$ for $m = 0, 1, 2, \ldots, 10$. The positions where field line tracing started are at $r_0 = 2.25$ and $z_0 = 0$, and seven field lines were traced starting at different θ angles. The field lines lie on four nested surfaces. Field lines started at $\theta_0 = \pi/4$ and $7\pi/4$ lie on the outer toroidal surface, field lines started at $\theta_0 = \pi/2$ and $3\pi/2$ lie on the next surface, field lines started at $\theta_0 = 3\pi/4$ and $5\pi/4$ lie on the next inner surface, and the field line started at $\theta_0 = \pi$ lies on the smallest toroidal surface. One should not try to fit a pattern to the field line starting points and the toroidal surface they lie on. As Fig. 12 shows, the toroidal surfaces change shape and position as a function of the angle θ. It was purely coincidence that we managed to choose (r_0, θ_0, z_0) so that more than one field line lie on a toroidal surface.

As was mentioned in the introduction, the solution of the Grad–Shafranov equation (5) leads to nested surfaces in the equilibrium MHD state. In cylindrical coordinates, these nested surfaces lie parallel to the cylindrical z-axis (Evangelidis 1981). Hu & Sonnerup (2001) reconstructed magnetic flux ropes in the solar wind from observational data using the Grad–Shafranov equation, and found nested surfaces parallel to the cylindrical axis that have non-circular cross-sections, as is the case in Fig. 12. In order to obtain nested flux surfaces of the same orientation to the cylindrical axis as in Fig. 12, we have to transform the coordinates from cylindrical to toroidal coordinates (Nishikawa & Wakatani 1994). Toroidal flux surfaces oriented perpendicular to the z-axis in cylindrical coordinates are unique to the solution presented in this paper.

The thickness of the shell of a torus can vary as a function of r and θ, as well as z. This occurred in a minority of cases that we found. One example of this is drawn in Fig. 13. These plots were produced with $C_m = 1$ for $m = 0, 1, 2, \ldots, 10$, $k_0 = 3\pi/2a_z$ and $k = 3$, which means that $\kappa = 2.759$. When the shell has a finite thickness, the magnetic field fills the shell as it rotates around

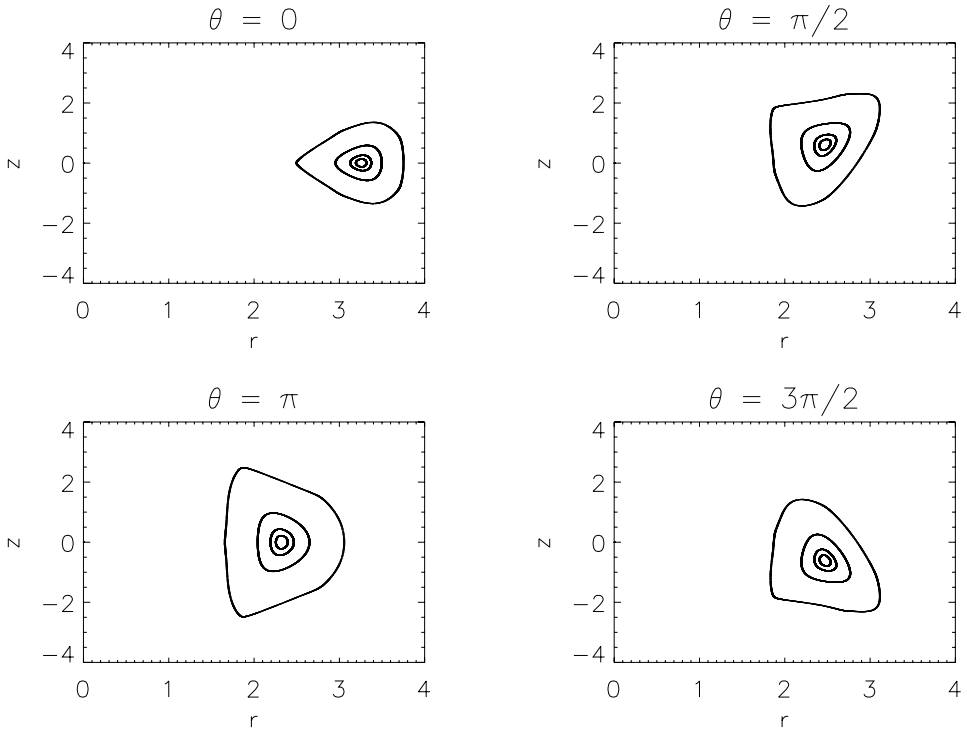

Figure 12. Some field lines lie on nested toroidal surfaces. Here seven field lines were followed for 10^3 revolutions in an anticlockwise direction around the z-axis. They lie on four nested toroidal surfaces, which are drawn on the (r, z) planes at angles $\theta = 0$, $\pi/2$, π and $3\pi/2$.

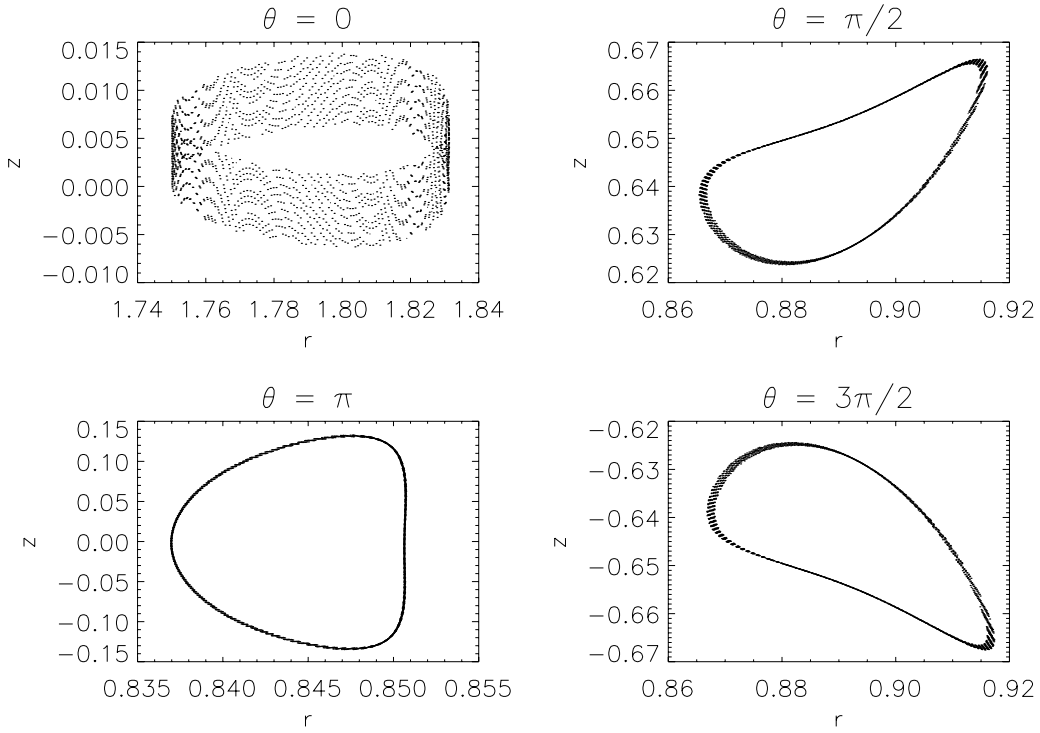

Figure 13. Broadening of the shell of the torus. A field line, initialized at $(r_0, \theta_0, z_0) = (1.75, 0, 0)$ is followed for 2000 rotations in an anticlockwise direction around the z-axis. The Cartesian (r, z) planes are drawn at angles $\theta = 0$, $\pi/2$, π and $3\pi/2$.

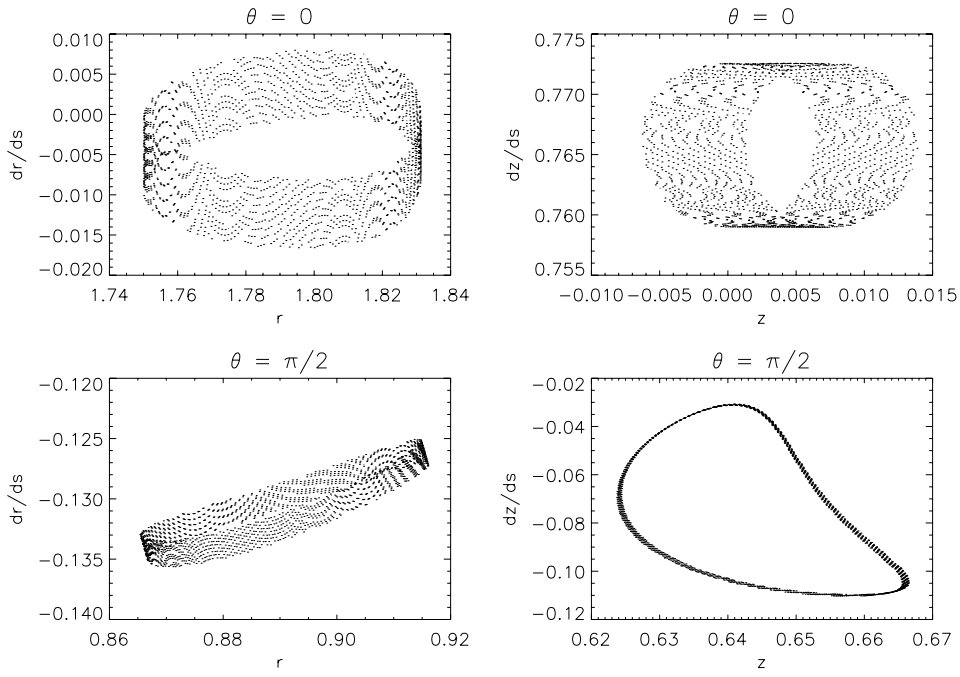

Figure 14. Poincaré plots $(r, \dot{r})$ and $(z, \dot{z})$ at the angles $\theta = 0$ and $\theta = \pi/2$ for the same plots as in Fig. 13.

the z-axis. We have found examples where the shell of the torus becomes thick enough at certain values of θ, so that the whole of the inside of the toroidal volume is filled by the magnetic field at those angles. Figs 14 and 15 are Poincaré plots of the magnetic field lines in Fig. 13 at the values of θ presented in Fig. 13. They show that we can consider the thickening of the toroidal shell as ergodic behaviour of the magnetic field lines. As in Cartesian space, the boundary of the ergodicity changes as we move around the z-axis.

5 CONCLUSION

We investigated a cylindrical solution of the linear force-free magnetic field, formulated in terms of Bessel and trigonometric

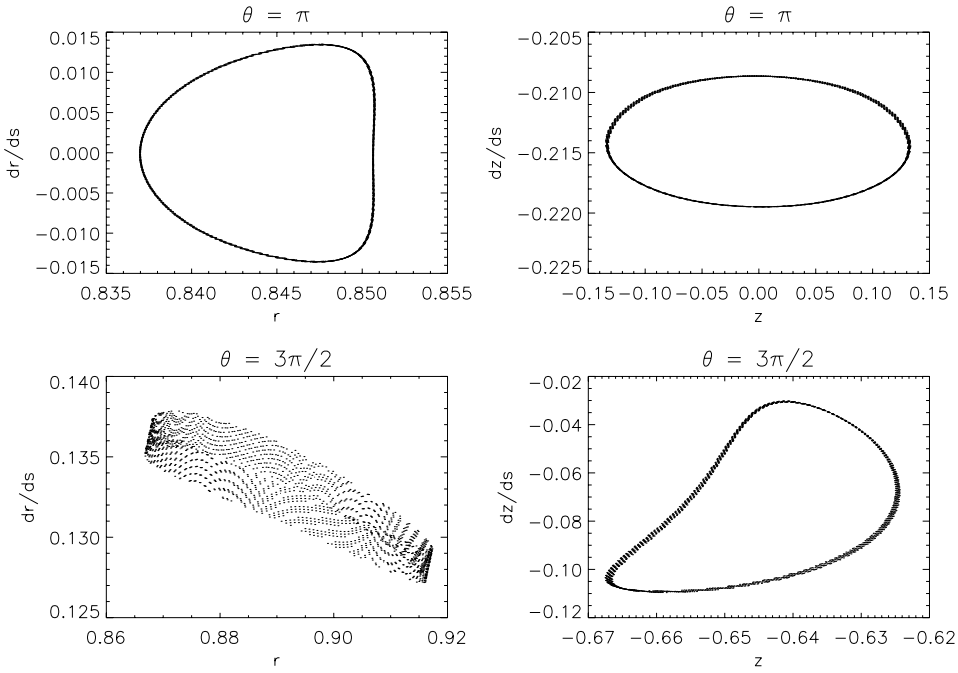

Figure 15. Poincaré plots $(r, \dot{r})$ and $(z, \dot{z})$ at the angles $\theta = \pi$ and $\theta = 3\pi/2$ for the same plots as in Fig. 13.

functions. The z-axis of the cylinder can be treated as either periodic or infinite, which allows modelling of low inverse aspect ratio tokamaks as well as magnetic flux tubes in the solar wind.

The simplicity of the analytical solution hides a wealth of field line topologies. By tracing the magnetic field lines numerically, we have found field lines that meander in three-dimensional (3D) space, as well as lines that remain on magnetic flux surfaces inside a finite cylindrical radius. These surfaces form tori that lie on, or close to, the (r, θ) plane perpendicular to the cylindrical z-axis. A search of the parameter space shows that these tori appear only within certain values of k in the linear force-free field equation (1), and that k is closely linked to the number of wavelengths k_0 chosen in the z-direction along the cylindrical axis. A systematic scan of the parameter values showed the existence of nested tori, as well as tori where the shell thickness varies as a function of position in 3D space.

We trust that the richness of the magnetic field structures will make this description of a linear force-free field a convenient tool in theoretical and numerical studies of magnetic flux tubes in space and laboratory plasmas.

ACKNOWLEDGMENTS

We would like to thank the anonymous referee for a critical and constructive report that improved the presentation of this paper.

REFERENCES

Alissandrakis C. E., 1981, A&A, 100, 197
Aly J. J., 1992, Solar Phys., 138, 133
Arnold V. I., 1965, Comptes Rendues de l'Acadèmie des Sciences, Paris, 261, 17
Aschwanden M. J., Nightingale R. W., Alexander D., 2000, ApJ, 541, 1059
Aschwanden M. J., Poland A. I., Rabin D. M., 2001, ARA&A, 39, 175
Barberio-Corsetti P., 1973, Plasma Phys., 15, 1131
Bellan P. M., 2003, Phys. Plasmas, 10, 1999
Berdichevsky D. B., Lepping R. P., Farrugia C. J., 2003, Phys. Rev. E, 67, 036405
Berger M. A., 1991, in Priest E. R., Hood A. W., eds, Advances in Solar System Magnetohydrodynamics. Cambridge Univ. Press, Cambridge, Chapter 11
Burlaga L. F., 1988, J. Geophys. Res., 93, 7217
Chandrasekhar S., 1956, Proc. Natl. Acad. Sci. USA, 42, 1
Chandrasekhar S., Kendall P. C., 1957, ApJ, 126, 457
Chandrasekhar S., Woltjer L., 1958, Proc. Natl. Acad. Sci. USA, 44, 285
Chiu Y. T., Hilton H. H., 1977, ApJ, 212, 873
Clegg J. R., Browning P. K., Laurence P., Bromage B. J. I., Stredulinsky E., 2000a, A&A, 361, 743
Clegg J. R., Browning P. K., Laurence P., Bromage B. J. I., Stredulinsky E., 2000b, J. Math. Phys., 41, 6783
Evangelidis E. A., 1981, Ap&SS, 75, 315
Evangelidis E. A., 1982, Ap&SS, 87, 117
Evangelidis E. A., Botha G. J. J., 2001, in Brekke P., Fleck B., Gurman J. B., eds, Proc. IAU Symp. 203, Recent Insights into the Physics of the Sun and Heliosphere: Highlights from SOHO and Other Space Missions. Astron. Soc. Pac., San Francisco, p. 270
Evangelidis E. A., Botha G. J. J., 2003, Solar Phys., 213, 69
Evangelidis E. A., Vaughan L. L., Botha G. J. J., 2000, Solar Phys., 193, 17
Farrugia C. J., Osherovich V. A., Burlaga L. F., 1995, J. Geophys. Res., 100, 12293
Ferron J. R., Walker M. L., Lao L. L., St. John H. E., Humphreys D. A., Leuer J. A., 1998, Nucl. Fusion, 38, 1055
Finn J. M., Guzdar P. N., Usikov D., 1994, ApJ, 427, 475
Gary G. A., 1989, ApJS, 69, 323
Gold T., Hoyle F., 1960, MNRAS, 120, 89
Golub L., Pasachoff J. M., 1997, The Solar Corona. Cambridge Univ. Press, Cambridge
Hansen W. W., 1935, Phys. Rev., 47, 139
Hu Q., Sonnerup B. U. Ö., 2001, Geophys. Res. Lett., 28, 467
Hundhausen A. J., 1995, in Kivelson M. G., Russell C. T., eds, Introduction to Space Physics. Cambridge Univ. Press, Cambridge, ch. 4
Lepping R. P. et al., 2001, Solar Phys., 204, 287
Lortz D., Spies G. O., 1994, Phys. Plasmas, 1, 249
Lothian R. M., Browning P. K., 2000, Solar Phys., 194, 205
Low B. C., 1977, ApJ, 212, 234

Low B. C., 1996, Solar Phys., 167, 217
Low B. C., 2001, J. Geophys. Res., 106, 25 141
Low B. C., Berger M. A., 2003, ApJ, 589, 644
Lundquist S., 1950, Arkiv för Fysik, 2, 361
Manheimer W. M., Lashmore-Davies C. N., 1989, *MHD and Microinstabilities in Confined Plasmas*. Adam Hilger, Bristol, p. 158, equation (14.23)
Marsh G. E., 1996, Force-Free Magnetic Fields. Solutions, Topology and Applications. World Scientific, Singapore
Martynov A. A., Medvedev S. Yu., 2002, Plasma Phys. Rep., 28, 259
Nagakawa Y., Raadu M. A., 1972, Solar Phys., 25, 127
Nishikawa K., Wakatani M., 1994, *Plasma Physics*. Springer-Verlag, Berlin, p. 178
Osherovich V. A., Farrugia C. J., Burlaga L. F., 1993, J. Geophys. Res., 98, 13225
Petrie G. J. D., Lothian R. M., 2003, A&A, 398, 287
Phillips K. J. H., 1992, Guide to the Sun. Cambridge Univ. Press, Cambridge
Priest E. R., 1982, Solar Magnetohydrodynamics. Kluwer, Dordrecht
Sakurai T., 1989, Space Sci. Rev., 51, 11
Salingaros N. A., 1990, Appl. Phys. Lett., 56, 617
Schönfelder A. O. Hood A. W., 1995, Solar Phys., 157, 223
Shimazu H., Vandas M., 2002, Earth Planets Space, 54, 783
Stangeby P. C., 2000, The Plasma Boundary of Magnetic Fusion Devices. IOP Publishing, Bristol
Taylor J. B., 1974, Phys. Rev. Lett., 33, 1139
Vandas M., Romashets E. P., 2003, A&A, 398, 801
Vandas M., Romashets E. P., Watari S., 2003, in Proc. ISCS 2003 Symp., ESA SP-535, Solar Variablility as an Input to the Earth's Environment. ESA Publications, Noordwijk, p. 583
Van der Linden R. A. M., Hood A. W., 1999, A&A, 346, 303
Wang H., Yan Y., Sakurai T., 2001, Solar Phys., 201, 323
Woltjer L., 1958, Proc. Natl. Acad. Sci. USA, 44, 489, 833
Zhugzhda Y. D., 1996, Phys. Plasmas, 3, 10

This paper has been typeset from a TEX/LATEX file prepared by the author.